Simultaneous molecular imaging of redox reactions monitored by Overhauser-enhanced MRI with ^{14}N- and ^{15}N-labeled nitroxyl radicals

Hideo Utsumi*, Ken-ichi Yamada, Kazuhiro Ichikawa, Kiyoshi Sakai, Yuichi Kinoshita, Shingo Matsumoto, and Mika Nagai

Department of Bio-Functional Science, Graduate School of Pharmaceutical Sciences, Kyushu University, Higashi-ku, Fukuoka 812-8582, Japan

MRI has provided significant clinical utility in the diagnosis of diseases and will become a powerful tool to assess phenotypic changes in genetically engineered animals. Overhauser enhanced MRI (OMRI), which is a double resonance technique, creates images of free radical distributions in small animals by enhancing the water proton signal intensity by means of the Overhauser effect. Several studies have demonstrated noninvasive assessment of reactive oxygen species generation in small animals by using low frequency electron spin resonance (ESR) spectroscopy/imaging and nitroxyl radicals. *In vivo* ESR signal intensities of nitroxyl radicals decrease with time after injection; and the decreases are enhanced by reactive oxygen species, generated in oxidative disease models in a site-specific manner. In this study, we show images of nitroxyl radicals with different isotopes by changing the external magnetic field for ESR irradiation between ^{14}N and ^{15}N nuclei in field-cycled OMRI. OMRI simultaneously obtained dual images of two individual chemical processes. Oxidation and reduction were monitored in a rate-dependent manner at nanometer scale by labeling membrane-permeable and -impermeable nitroxyl radicals with ^{14}N and ^{15}N nuclei. Phantom objects containing ascorbic acid-encapsulated liposomes with membrane-permeable radicals but not membrane-impermeable ones show a time-dependent decrease of the OMRI image intensity. The pharmacokinetics in mice was assessed with OMRI after radical administration. This OMRI technique with dual probes should offer significant applicability to nanometer scale molecular imaging and simultaneous assessment of independent processes in gene-modified animals. Thus, it may become a powerful tool to clarify mechanisms of disease and to monitor pharmaceutical therapy.

ESR | reactive oxygen species | oxidative disease | nanometer

Anatomic imaging modalities such as MRI, ultrasound, positron emission tomography, and x-ray computerized tomography (CT) have provided significant clinical utility in the diagnosis of diseases as well as help in monitoring treatment repeatedly and noninvasively (1). Information from such techniques is predominantly morphological in nature, which can, based on the architectural differences between normal and pathological conditions, identify disease states. Additional information related to physiological/metabolic processes is obtained. With recent advances in imaging instrumentation as well as novel concepts in the design of contrast media, imaging of molecular events is rapidly emerging as a major field (2). In small animal imaging research, the importance of molecular imaging has assumed a major role, especially because the cost of certain genetically engineered animal models is high. Consequently noninvasive assessment of phenotypic changes is an advantage compared with killing the animals for histological examination. Molecular imaging research is driven by advances in both imaging modalities as well as the development of novel imaging beacons that can monitor specific cellular/intracellular pro-

cesses from which pathologies can be mapped out in specific regions of the body versus time.

Nitroxyl radicals, which belong to the six-membered piperidine (TEMPO) or the five-membered pyrrolidine (PROXYL) class, are stable organic free radicals, are less toxic, and even serve as *in vitro* (3, 4) and *in vivo* antioxidants (5–7). In addition to these useful features, nitroxyl radicals, by virtue of their paramagnetic nature, having a single unpaired electron, serve as imaging probes in techniques such as *in vivo* electron spin resonance (ESR) spectroscopy/imaging. Nitroxyl radicals have similar redox potentials to that of redox enzymes (8), and are reduced to the corresponding hydroxylamine, resulting in ESR signal loss (9). The ESR signal loss was also observed in the reaction of nitroxyl radicals with reactive oxygen species (ROS) (3, 10). Several *in vivo* ESR studies using nitroxyl radicals as probes were carried out in our laboratory and others to obtain useful physiological information and to assess ROS generation in oxidative disease models (10–15). Nitroxyl radicals can be derivatized to achieve specific cellular/subcellular localizing capabilities while retaining the simple spectral features useful in imaging (16, 17). Additionally, isotopic substitution of the nitrogen atom from the naturally abundant ^{14}N to ^{15}N provides enhanced detection sensitivity by decreasing the spectral multiplicity. ESR imaging (ESRI) provides the spatial distribution of the nitroxyl radical whereas anatomic information is not available (18–22). The spatial resolution of an ESRI image is poorer than that of MRI because of the large ESR line-width. It is usually at the mm level unless high field gradients are used.

Overhauser-enhanced MRI (OMRI) is a double resonance technique that uses the presence of paramagnetic agents to enhance the signal intensity from nuclear spins by means of a process known as dynamic nuclear polarization (DNP) or Overhauser effect (23–28). In this phenomenon, the relatively stronger magnetic moment of the electron is used to enhance the polarization of the nuclear spins, thereby enhancing their signal. The unique advantage of this technique is high spatial resolution of the image and short acquisition time. The significant contrast-to-noise ratio obtained by this technique makes OMRI advantageous in obtaining physiological information. Lurie *et al*. (23) used nitroxyl radicals and successfully obtained images of tissue water protons in the vicinity of the paramagnetic radical and so achieved *in vivo* imaging. More recent studies used this concept

to provide *in vivo* pO$_2$ maps (24) as well as to hyperpolarize endogenous ^{13}C-containing molecules for *in vivo* molecular imaging applications (29). The OMRI technique can exploit the spectral wealth available in the ESR spectra of paramagnetic molecules to obtain functional information from images such that events at a molecular level (nanometer level) can be perceived by using the chemical flexibility of the nitroxyl probe design in the following way: (*i*) nitroxyl radicals such as PROXYLs can be substituted at the 3-position to direct the contrast agent to specific cellular/subcellular regions; and (*ii*) the nitrogen nucleus of the nitroxyl radicals containing ^{14}N nuclei has a characteristically different DNP spectrum compared with the ^{15}N-substituted molecule. The presence of both species, which, if targeted to different cellular regions, can be simultaneously imaged by using OMRI.

In this study, we demonstrate the capability to simultaneously image two different but related reactions and implement this technique in an *in vivo* model. Such capabilities will be of significant use in studies of experimental models of diseases related to oxidative stress and aging in various organs by using the inherent antioxidant properties of this class of agents and the responses they provide in imaging modality.

Results

Fig. 1*A* shows the structure and the sites of isotopic differences in the nitrogen nuclei of the nitroxyl ring of the PROXYL probes. Compound **1** is a PROXYL with ^{14}N nuclei whose ESR spectrum exhibited three lines, characteristic of an unpaired electron interacting with a ^{14}N nucleus ($I = 1$), whereas compound **2** is the PROXYL derivative with ^{15}N nuclei substituted for ^{14}N and exhibits an ESR spectrum with a doublet hyperfine splitting (data not shown). The pulse sequence used to simultaneously detect DNP effects by using ^{14}N- and ^{15}N-labeled nitroxyls is shown in Fig. 1*B*. The pulse sequence corresponding to detection of ^{14}N nuclei is shown schematically on the left side of the dotted line where ESR magnetic field (B_0^{ESR}) (^{14}N) is used to irradiate the low field transition of the triplet ESR spectrum of compound **1**. On the right side of the dotted line B_0^{ESR} (^{15}N) corresponds to the low field transition of the doublet ESR spectrum of compound **2**. Fig. 1 *C* and *D* shows the corresponding DNP spectra of compounds **1** and **2** obtained by detecting the proton intensities after ESR irradiation at appropriate magnetic fields in the range of 5–10 mT, thereby spanning the ESR spectra of the nitroxyl species. The ^{14}N and ^{15}N hyperfine coupling constants obtained from the DNP spectra for the two nitroxyls (compound **1** and compound **2**) are in close agreement with the corresponding hyperfine coupling constants measured in their ESR spectra. Fig. 1*E* shows the DNP spectrum obtained when both nitroxyls were tested simultaneously. The DNP spectrum obtained from the mixture shows that both species can be detected simultaneously and also distinguished from each other with adequate spectral resolution. Fig. 1 *F* and *G* shows the dependence of the enhancement of the proton intensity from the DNP spectrum as a function of concentration of both these agents. As can be seen, the proton signal enhancement depends on the concentration of the nitroxyl up to 2 mM. Beyond this concentration, a modest deterioration of the signal was observed (data not shown) that may be associated with the spectral broadening typical at higher concentrations. However, at a given concentration, the proton signal enhancement was higher for ^{15}N-labeled PROXYL when compared with the ^{14}N-labeled analog because of the reduced spectral multiplicity of the $I = 1/2$ nucleus.

To examine the imaging capabilities where both nitroxyl spin probes can be simultaneously imaged, a phantom containing both probes in several different tubes was tested. The arrangement of the probes in the redox and nanoscale imaging phantom are shown in Figs. 2*A* and 3*A*. In Fig. 2*A*, the three tubes
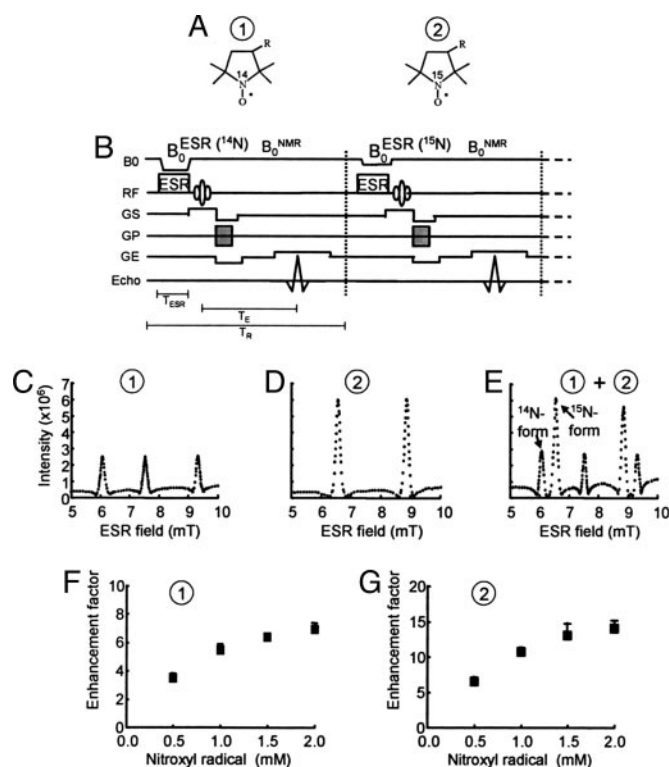

Fig. 1. DNP of ^{14}N- and ^{15}N-labeled PROXYLs. (*A*) Chemical structures of ^{14}N- and ^{15}N-nitroxyl radicals. (*B*) Field-cycle OMRI pulse sequence for the simultaneous separate imaging of ^{14}N- and ^{15}N-nitroxyl radicals. (*C–E*) DNP spectra of ^{14}N-, ^{15}N-nitroxyl radical, and both, respectively. (*F* and *G*) Dose-response curves of DNP intensities for ^{14}N- and ^{15}N-nitroxyl radicals, respectively. The OMRI experiments were performed on a custom-built (Philips Research Laboratories, Hamburg, Germany) human whole-body magnet (79 cm diameter; 125 cm length). The resonator assembly consists of the NMR transmit saddle coil (25 cm diameter, 23 cm length), a solenoidal receive coil (5 cm i.d., 60 mm length), and the ESR saddle coil (13. 5 cm diameter, 23.5 cm length). The pulse sequence started with the ramping B_0^{ESR}, which was followed by switching on the ESR irradiation (220.6 MHz), and the associated field gradients were turned on under B_0^{NMR}. Typical scan conditions in OMRI are $T_R/T_E/T_{ESR}$: 1,200 ms/25 ms/600 ms. DNP spectra of 2 mM aqueous solution of ^{14}N-carbamoyl-PROXYL (*C*) and ^{15}N-carbamoyl-PROXYL (*D*), and the mixture of ^{14}N- and ^{15}N-carbamoyl-PROXYL (*E*) were obtained by changing B_0^{ESR} between 5–10 mT with the sequence shown in *A*, and the intensities of DNP of ^{14}N-carbamoyl-PROXYL (*F*) and ^{15}N-carbamoyl-PROXYL (*G*) are plotted against their concentration.

containing the ^{15}N-labeled carbamoyl-PROXYL (3-carbamoyl-2,2,5,5-tetramethyl-pyrrolidine-1-oxyl) radical in ascorbic acid (AsA) solution are represented by red circles, and the other three tubes containing the ^{14}N-labeled carbamoyl-PROXYL hydroxylamine in horseradish peroxidase (HRP)/H$_2$O$_2$ solution are shown in blue. AsA can reduce nitroxyl radicals to the corresponding hydroxylamines rapidly, and HRP/H$_2$O$_2$ can oxidize hydroxylamine to the corresponding nitroxyl radical (9). Thus, the tubes containing ^{15}N-carbamoyl-PROXYL (red circles) are expected to undergo time-dependent intensity decreases, whereas the ^{14}N-labeled PROXYL hydroxylamine (blue circles) exhibit time-dependent increases in image intensity. OMRI scans were carried out as a function of time on the phantoms, as shown in Fig. 2*B*. The image data show that the intensity from the tubes containing the ^{15}N-nitroxyl radical in the presence of AsA gradually decreased with time (indicated with red in Fig. 2*B*), whereas the image intensity from tubes containing ^{14}N-hydroxylamine increased in a dose-dependent manner (indicated with blue in Fig. 2*B*). Fig. 2*C* displays the images of decreasing and increasing rate constants of the image intensities. The rate
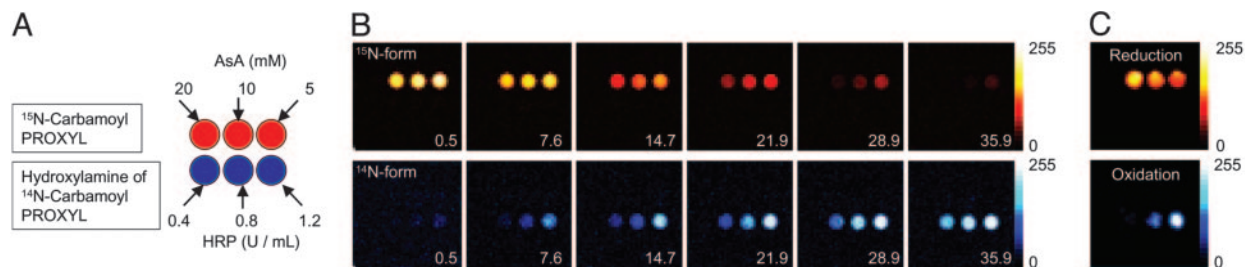
Fig. 2. Simultaneous images of two independent chemical processes (oxidation and reduction) using the nitroxyl radical and its reduced form. (*A*) Six phantom tubes were used for different process OMRI images, three tubes (red color) contain 2 mM ^{15}N-carbamoyl-PROXYL and various concentrations of AsA, and the remaining three tubes (blue color) contain 5 mM ^{14}N-carbamoyl-PROXYL hydroxylamine, different amounts of HRP, and 5 mM hydrogen peroxide. (*B*) Time-dependent OMRI Image of ^{15}N-compounds (red) and ^{14}N-compounds (blue). (*C*) The image of decay rates for ^{15}N-carbamoyl-PROXYL and increasing rates of ^{14}N-carbamoyl-PROXYL hydroxylamine were calculated assuming first-order kinetics of the time-dependent decrease/increase of the contrast (Fig. 2*B*). OMRI was performed as described in the legend of Fig. 1 (FOV, 48 × 48 mm; matrix, 64 × 64; slice thickness, 10 mm; $T_R/T_E/T_{ESR}$, 1,200 ms/25 ms/600 ms).

constant images clearly show dose dependence. When the rates of image intensity loss and gain from each pixel are estimated and displayed, one obtains a parametric image of the rate of intensity loss or gain, respectively. Because nitroxyl radicals and the corresponding hydroxylamine have been found to be reduced or oxidized by their reaction with redox enzymes, respectively, the present OMRI studies suggest the possibility of monitoring reducing and oxidizing processes noninvasively.

To demonstrate molecular imaging at a nanometer scale with OMRI, seven phantom tubes were prepared as shown in Fig. 3*A*. Of the six outer tubes, two containing the ^{15}N compounds are shown with red, whereas two containing the ^{14}N compounds are shown with blue. Two of the outer tubes contained both carboxy-PROXYL (3-carboxy-2,2,5,5-tetramethyl-pyrrolidine-1-oxyl) and MC-PROXYL (3-methoxycarbonyl-2,2,5,5-tetramethyl-

Fig. 3. Simultaneous and time-dependent OMRI of ^{15}N/^{14}N-carboxy-PROXYL and ^{15}N/^{14}N-MC-PROXYL in liposomes encapsulating AsA (100 mM). Seven phantom tubes containing ^{14}N-labeled and/or ^{15}N-labeled nitroxyl radicals in the presence and the absence of liposomes, which are shown in Fig. 3*A*, were placed in the OMRI so that images of ^{15}N- and ^{14}N-enhanced images (red and blue, respectively, in Fig. 3*B*) were obtained simultaneously at the times shown in the figures. The presence of ^{15}N-carboxy-PROXYL and ^{15}N-MC-PROXYL are clearly shown by the red color, and ^{14}N-carboxy-PROXYL and ^{14}N-MC-PROXYL by the blue color (Fig. 3*B*). (*C*) The images of the decay rates for ^{14}N- and ^{15}N-enhanced OMRI images were calculated by assuming first-order kinetics for the time-dependent decrease of the contrast (Fig. 3*B*). Only MC-PROXYL showed decay images in both ^{14}N- and ^{15}N-enhanced OMRI. OMRI was performed as described in the legend of Fig. 1 (FOV, 48 × 48 mm; matrix, 64 × 64; slice thickness, 10 mm; $T_R/T_E/T_{ESR}$, 1,200/25/600 ms.

pyrrolidine-l-oxyl), and are indicated by the red and blue stripes. The tubes circled with a bold line contained liposomes encapsulated with 100 mM AsA. The central white tube contained no liposomes. Here, carboxy-PROXYL does not penetrate liposome membrane whereas the MC-PROXYL can permeate freely back and forth across the membrane and undergo 1-electron reduction to the corresponding hydroxylamine. Thus, tubes containing carboxy-PROXYL are not expected to undergo time-dependent intensity changes, whereas the MC-PROXYL can change its image intensity. OMRI scans were carried out as a function of time on the phantom tubes. Three such images at 2.9 min, 13.9 min, and 24.9 min are shown in Fig. 3*B*. The image data show that the intensity from the tubes containing MC-PROXYL in the presence of AsA-encapsulating liposomes gradually decreased with time, whereas the image intensities from tubes containing carboxy-PROXYL were constant. The rate of intensity loss from each pixel clearly represents the nanometer scale imaging between liposomal membranes (Fig. 3*C*). It is worth noting that the rate of intensity loss in the tube containing both MC- and carboxy-PROXYL (indicated with stripes in Fig. 3*A*) was the same as that in the tube containing either MC- or carboxy-PROXYL. Because nitroxyl radicals have been found to react with ROS and lose their paramagnetism, the present OMRI studies suggest that sites of ROS production can be monitored noninvasively.

Results from these phantom studies suggest that, if two nitroxyl radicals with different isotopic substitution and different ring substituents (which direct them to different subcellular regions) lose or gain their paramagnetism, then their oxidation and reduction can be spatially resolved and distinguished. Accordingly, with judicious choice of the spin probe and isotopic substitution, this technique allows one to perceive changes at nanometer scale, even though the intrinsic spatial resolution of the image acquisition modality is ≈0.1 mm.

To test the feasibility of *in vivo* imaging simultaneously, ^{15}N-labeled oxo-TEMPO (4-oxo-2,2,6,6-tetramethyl-piperidine-1-oxyl) was administered intragastrically and ^{14}N-labeled carbamoyl-PROXYL was injected intravenously. Furthermore, in both cases, six fiducial markers were placed to permit coregistration of both images (three capillaries each for ^{15}N and ^{14}N nitroxyls) along with the conventional proton-based MRI images collected at 0.2 T. The anatomic images obtained by using the T_1-enhanced sequence at 0.2 T are shown in Fig. 4 in a gray scale. The OMRI images using the interleaved ESR excitation sequence to alternately excite the ^{15}N-labeled oxo-TEMPO and the ^{14}N-labeled carbamoyl-PROXYL are shown in Fig. 4 *A* or *B* with a red or blue color scale, respectively. Four separate images after the administration of the nitroxyl radicals were collected at different time points: 1.5, 4.5, 7.5, and 11.5 min. As can be seen, the intragastrically administered nitroxyl probe was found to be
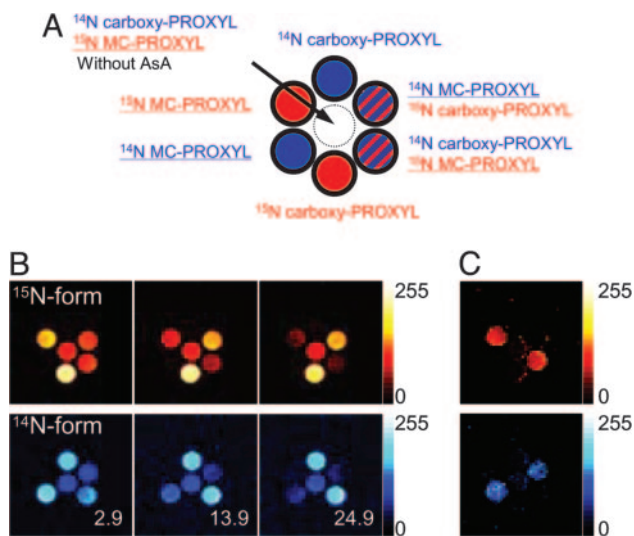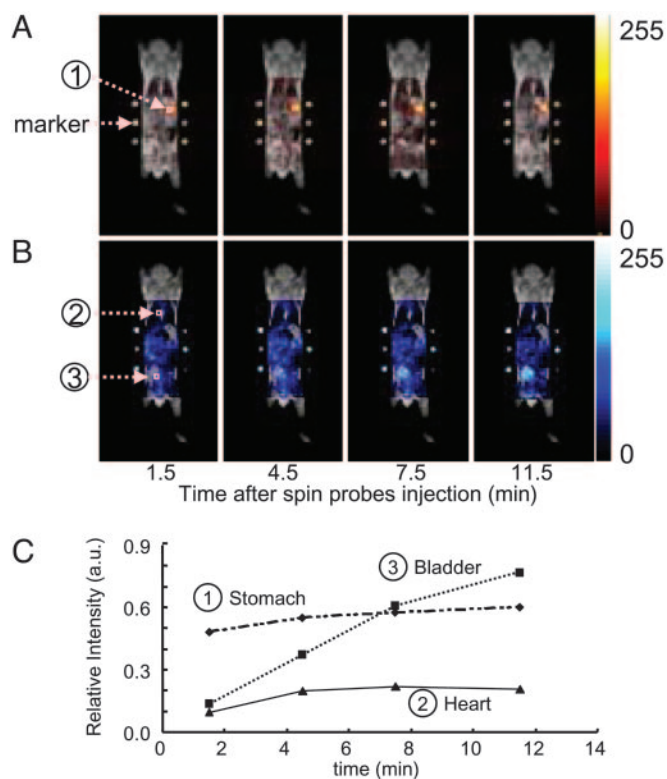
Fig. 4. Pharmacokinetic images of ^{14}N- and ^{15}N-nitroxyl probes after injection through different routes. The time-dependent simultaneous images of ^{15}N-oxo-TEMPO (*A*) and ^{14}N-carbamoyl-PROXYL (*B*) in a living mouse after intragastrical and i.v. injection, respectively, and the time course of image intensities at stomach, heart, and bladder (*C*). Into a living mouse, 200 μl of ^{15}N-oxo-TEMPO (10 mM) was administered intragastrically, and then 200 μl of ^{14}N-carbamoyl-PROXYL (300 mM) i.v. Immediately after administrations, OMRI images of ^{14}N- and ^{15}N-nitroxyl radicals were obtained as described in Fig. 1. T_1-weighted MRI was performed on a clinical MRI instrument, and the OMRI images were superimposed with the MRI image by fitting the position of the markers (six capillaries containing either radical) (FOV, 48 × 48 mm; matrix, 64 × 64; slice thickness, 30 mm; $T_R/T_E/T_{ESR}$, 1,100 ms/25 ms/550 ms).

confined to the site where it was deposited during the imaging time, whereas the intravenously administered spin probe exhibited a global distribution over the mouse. To better understand the temporal profile of the distribution of the probes, regions of interest were chosen, and the intensity changes versus time are shown in Fig. 4*C*. The data reveal that, whereas changes in intensity of the intragastrically administered nitroxyl were minimal, the intravenously administered nitroxyl showed changes dependent on the organ/region examined. Although minimal changes were evident in the cardiac tissue, a progressively increasing level of the nitroxyl was noticed in the bladder region, indicative of the renal excretion of the probe molecule. These studies prove that it is possible to track two independent molecules with potential antioxidant properties simultaneously and that their distribution can be coregistered with anatomic images. This capability allows one to examine the role that ROS play in tissue damage noninvasively by using imaging probes such as nitroxyls, which are also effective antioxidants.

Discussion

Several studies from our laboratory and others used nitroxyl radicals to image their distribution and monitor tissue redox as well as ROS generation *in vivo* and noninvasively by using ESR imaging at low frequency (0.3–1.2 GHz) in small animals (10–15). The spatial resolution depended on the ESR spectral line width ($\approx$3 MHz), which is typically 2–3 orders greater than that for ^{1}H NMR. This image resolution restricts the number of species that can simultaneously be administered and imaged. However, nitroxyl radicals offer unique opportunities for imaging by virtue of three important features: (*i*) stable nitroxyl radicals undergo reduction to diamagnetic species by accepting reducing equivalents from cellular redox systems (9), or by electron transfer reactions with ROS (10, 30); (*ii*) nitroxyl radicals can be substituted with groups that direct them to specific regions *in vivo* (16); (*iii*) isotopic substitution of nitroxyls with ^{15}N can provide distinct spectral features compared with ^{14}N-labeled nitroxyls, because imaging techniques can distinguish ^{15}N from ^{14}N-labeled probes *in vivo*.

OMRI is uniquely capable of providing anatomically coregistered images that can also display spin probe distributions. Several studies have used nitroxyl radicals (23, 31) and trityl radicals (24–26) to obtain images with useful spatial resolution and also to discern functional information. We tested the possibility of whether OMRI had sufficient spectral resolution in the ESR excitation mode to detect simultaneously ^{14}N- and ^{15}N-labeled nitroxyl radicals. Phantom studies were designed to examine this capability. Results from this study show that indeed two separate molecules of nitroxyl radicals can be simultaneously detected by OMRI and their spatial distributions obtained. Further, the temporal resolution of this imaging modality utilizes time-efficient pulse sequences now routinely available in MRI and can be used to monitor independent chemical reactions simultaneously. The time-dependent signal loss of the OMRI image was observed when the nitroxyl radicals, which are capable of permeating the liposomal bilayer, get reduced, whereas the nitroxyl agent incapable of crossing the membrane bilayer remained intact and signal loss of the OMRI images was not observed. This capability demonstrates that OMRI combined with dual labeled nitroxyl spin probes allows one to perceive and distinguish events occurring at a nanometer scale, even though the intrinsic image resolution is $\approx$0.1 mm.

This capability further exploits the fact that nitroxyl radicals are efficient antioxidants that also provide protection against oxidative stress in several modalities. More recently, these radicals have been shown effective in humans in inhibiting ionizing radiation-induced normal tissue toxicity (32). The beneficial antioxidant property can also be used with noninvasive imaging techniques to probe sites of oxidative stress. For example, it is possible to track the ROS generation in adjuvant arthritis model because nitroxyl radicals are capable of reacting with ROS produced in arthritis (33). Because the spectra of nitroxyl radicals arise from the region in which they accumulate, it is possible to image their localization, as has been shown by using ESR imaging (11, 16). Another unique feature of this technique is that it is possible to monitor independent chemical reactions by using the double probe method, for example, oxidation reactions (time-dependent oxidation of hydroxylamine to the corresponding nitroxyl radical) as well as reduction reactions (reduction of nitroxyl radical to the corresponding hydroxylamine). Therefore, not only is it possible to monitor two separate probes simultaneously, but also the processes in which they participate can be assessed noninvasively. Such techniques have potential to fill the need to observe phenotypic changes in genetically modified experimental animals, where currently such changes are usually studied in terminal experiments, involving killing the animals for tissue examination.

Several developments in this field are possible with this method in terms of instrumentation, image data acquisition, and probe design, making possible a more robust and useful technique for various applications. Resonator assemblies that can specifically irradiate regions of interest to achieve higher signal/noise (SNR) and prepolarization strategies where the protons can be polarized outside the OMRI scanner more effectively are

ztwo avenues to be explored. With regard to probes, selective deuteration of the nitroxyl ring will enhance the SNR and thereby improve spatial and temporal resolutions. Image data acquisition strategies where minimal data can be acquired without compromising image quality will also contribute to an overall optimization of this modality.

Materials and Methods

Scanner. The OMRI experiments were performed on a custom-built (Philips Research Laboratories, Hamburg) human whole-body magnet (79 cm diameter; 125 cm length) (24), which was modified in the pulse sequence according to our request, by using a standard spin warp gradient echo sequence for MRI as shown in Fig. 1B, where each phase encoding step was preceded by an ESR saturation pulse to elicit the Overhauser effect. To avoid excess power deposition during the ESR cycle, the external magnetic field was operated in a field-cycled mode, the B_0^{ESR} was at 6.103 mT and 6.563 mT for the ^{14}N-compound and ^{15}N-compound, respectively, and B_0^{NMR} was 14.552 mT. For NMR, the resonator assembly to study mice was tuned to 617 kHz and consisted of a transmit saddle coil (25 cm diameter, 23 cm length) and a solenoidal receive coil (5 cm i.d., 6 cm length). For ESR, a saddle coil (13. 5 cm diameter, 23.5 cm length) tuned to 220.6 MHz and concentric to the NMR coils was used.

In this work, the images of ^{14}N and ^{15}N nitroxyl radicals were constructed with the data of ^{14}N and ^{15}N nitroxyl radicals in k-space obtained by changing magnetic field at each phase encode (step, 64). The pulse sequence started with ramping of the B_0 field to either 6.103 mT or 6.563 mT, corresponding to the ESR irradiation. It was followed by switching on the ESR irradiation for a period of ≈600 ms. Then B_0 was ramped to 14.552 mT before the rf pulse and the associated field gradients were turned on. Also, at the beginning or end of the cycle, a conventional MRI (without ESR on) was collected for computing the enhancement factors. A Hewlett-Packard PC (operating system, LINUX 5.2) was used for data acquisition. The images were reconstructed from the echoes by using standard software and were stored in DICOM format (Digital Imaging and Communications in Medicine). Further image processing, such as the decay rate calculation, was done with programs coded in MATLAB. Typical scan conditions in OMRI are repetition time (T_R)/echo time (T_E)/ESR irradiation time (T_{ESR}): 1,200 ms/25 ms/600 ms; no. of averages = 1; 64 phase-encoding steps. The pixel size was 0.63 mm × 0.63 mm with a slice thickness of 10 mm. The image field of view, 48 mm, was represented by a 64 × 64 matrix.

DNP spectra of 2 mM aqueous solutions of ^{14}N- and ^{15}N-carbamoyl-PROXYL, and the mixture of ^{14}N- and ^{15}N-carbamoyl-PROXYL were obtained by varying B_0^{ESR} between 5–10 mT with the sequence shown in Fig. 1B.

Nitroxyl Probes. Oxo-TEMPO, carboxy-PROXYL, and carbamoyl-PROXYL were purchased from Aldrich. MC-PROXYL was synthesized as described (34). ^{15}N-labeled nitroxyl probes were synthesized with ^{15}N-ammonium chloride (Cambridge Isotope Laboratories, Cambridge, MA) in our laboratory by using a literature procedure (35), and no contamination of ^{14}N was confirmed with ESR spectroscopy. All other chemicals were commercially available reagent grade quality.

Redox Phantom Studies of Two Different Processes. Of six phantom tubes, three contained 2 mM ^{15}N-carbamoyl-PROXYL and

various concentrations of AsA as reductant. The remaining three tubes contained 5 mM the corresponding hydroxyl amine of ^{14}N-carbamoyl-PROXYL, 5 mM hydrogen peroxide, and various amounts of HRP, which were used as oxidant. The six tubes, shown in Fig. 2A, were placed in the OMRI resonator. The images of ^{14}N- and ^{15}N-enhanced images were obtained simultaneously at the times shown with blue and red colors in the figures, respectively. The images of the rate changes for ^{14}N- and ^{15}N-carbamoyl-PROXYL were calculated by assuming first-order kinetics for the time-dependent change in contrast. The OMRI experiments were performed as described in the legend of Fig. 1 [field of view (FOV) 48 × 48 mm; matrix, 64 × 64; slice thickness,10 mm; $T_R/T_E/T_{ESR}$, 1,200 ms/25 ms/600 ms].

Nano-Scale (Inside and Outside of Liposomal Membranes) Phantom Studies. Seven phantom tubes for nano-scale imaging are shown in Fig. 3A. Blue and red colors indicate the ^{14}N-compound and ^{15}N-compound, respectively. The six outer tubes contain either or both the ^{14}N-compound and the ^{15}N-compound entrapped in liposomes. They also contained 100 mM AsA and were prepared with egg yolk phosphatidyl choline as described (36). The center tube contains both the ^{14}N-compound and the ^{15}N-compound but without the liposomes. The seven phantom tubes were placed in the OMRI so that the images of the ^{14}N- and ^{15}N-enhanced images were obtained simultaneously at the times shown in the figures. The images of the decay rates for ^{14}N- and ^{15}N-PROXYL were calculated by assuming first-order kinetics for the time-dependent decrease of contrast. The OMRI experiments were performed as described in the legend of Fig. 1 (FOV, 48 × 48 mm; matrix, 64 × 64; slice thickness, 10 mm; $T_R/T_E/T_{ESR}$, 1,200 ms/25 ms/600 ms).

Animal Studies. Male ddy mice (5 weeks old) were purchased from Seac Yoshitomi Co. (Fukuoka, Japan) and were acclimatized for one week before experimentation. Diet (MF, Oriental Yeast Co., Tokyo) and water were provided ad libitum. The animals were fasted for 24 h with free access to water until 1 h before the experiment. After anesthetization by Nembutal (Dainabot Co., Tokyo), 200 μl of ^{15}N-oxo-TEMPO (10 mM) was administered orally and then 200 μl of ^{14}N-carbamoyl-PROXYL (300 mM) intravenously. Immediately after administrations, OMRI images of ^{14}N- and ^{15}N-nitroxyl radicals were obtained as described in Fig. 1 (FOV, 48 × 48 mm; matrix, 64 × 64; slice thickness, 30 mm; $T_R/T_E/T_{ESR}$, 1,100 ms/25 ms/550 ms).

The conventional MRI experiments were performed on a 0.2 T MRI (Hitachi Medical Corporation, Tokyo) by using a standard T_1-weighted enhanced pulse sequence. The OMRI images were superimposed with the image of the MRI by fitting the position of the markers (the six capillaries containing the radicals).

All procedures and animal care were approved by the Committee on Ethics of Animal Experiments, Graduate School of Pharmaceutical Sciences, Kyushu University, and were conducted according to the Guidelines for Animal Experiments of the Graduate School of Pharmaceutical Sciences, Kyushu University.

1. Hildebrandt, I. J. & Gambhir, S. S. (2004) *Clin. Immunol.* **111,** 210–224.
2. Massoud, T. F. & Gambhir, S. S. (2003) *Genes Dev.* **17,** 545–580.
3. Krishna, M. C., Russo, A., Mitchell, J. B., Goldstein, S., Dafni, H. & Samuni, A. (1996) *J. Biol. Chem.* **271,** 26026–26031.
4. Miura, Y., Utsumi, H. & Hamada, A. (1993) *Arch. Biochem. Biophys.* **300,** 148–156.
5. Hahn, S. M., Sullivan, F. J., DeLuca, A. M., Krishna, M. C., Wersto, N., Venzon,

D., Russo, A. & Mitchell, J. B. (1997) *Free Radical Biol. Med.* **22,** 1211–1216.
6. Li, H., Ma, L., Hsia, C. J., Zweier, J. L. & Kuppusamy, P. (2002) *Free Radical Biol. Med.* **32,** 712–719.
7. Miura, Y., Hamada, A. & Utsumi, H. (1995) *Free Radical Res.* **22,** 209–214.
8. Kato, Y., Shimizu, Y., Lin, Y. J., Unoura, K., Utsumi, H. & Ogata, T. (1995) *Electrochim. Acta* **40,** 2799–2802.

9. Kocherginsky, N. & Swartz, H. M. (1995) in *Nitroxide Spin Labels: Reactions in Biology and Chemistry*, eds. Kocherginsky, N. & Swartz, H. M. (CRC, Boca Raton, FL), pp. 27–66.
10. Kasazaki, K., Yasukawa, K., Sano, H. & Utsumi, H. (2003) *Free Radical Res.* **37,** 757–766.
11. Yamato, M., Egashira, T. & Utsumi, H. (2003) *Free Radical Biol. Med.* **35,** 1619–1631.
12. Takeshita, K., Takajo, T., Hirata, H., Ono, M. & Utsumi, H. (2004) *J. Invest. Dermatol.* **122,** 1463–1470.
13. Kuppusamy, P., Li, H., Ilangovan, G., Cardounel, A. J., Zweier, J. L., Yamada, K., Krishna, M. C. & Mitchell, J. B. (2002) *Cancer Res.* **62,** 307–312.
14. Halpern, H. J., Chandramouli, G. V., Barth, E. D., Yu, C., Peric, M., Grdina, D. J. & Teicher, B. A. (1999) *Cancer Res.* **59,** 5836–5841.
15. Gallez, B., Bacic, G., Goda, F., Jiang, J., O'Hara, J. A., Dunn, J. F. & Swartz, H. M. (1996) *Magn. Reson. Med.* **35,** 97–106.
16. Sano, H., Naruse, M., Matsumoto, K., Oi, T. & Utsumi, H. (2000) *Free Radical Biol. Med.* **28,** 959–969.
17. Anzai, K., Saito, K., Takeshita, K., Takahashi, S., Miyazaki, H., Shoji, H., Lee, M. C., Masumizu, T. & Ozawa, T. (2003) *Magn. Reson. Imaging* **21,** 765–772.
18. Matsumoto, S., Nagai, M., Yamada, K., Hyodo, F., Yasukawa, K., Muraoka, M., Hirata, H., Ono, M. & Utsumi, H. (2005) *Concepts Magn. Reson. Part B (Magn. Reson. Engineering)* **25B,** 1–11.
19. He, G., Deng, Y., Li, H., Kuppusamy, P. & Zweier, J. L. (2002) *Magn. Reson. Med.* **47,** 571–578.
20. Di Giuseppe, S., Placidi, G. & Sotgiu, A. (2001) *Phys. Med. Biol.* **46,** 1003–1016.
21. Sato, T., Oikawa, K., OhyaNishiguchi, H. & Kamada, H. (1997) *Rev. Sci. Instrum.* **68,** 2076–2081.
22. Halpern, H. J., Peric, M., Yu, C., Barth, E. D., Chandramouli, G. V., Makinen, M. W. & Rosen, G. M. (1996) *Biophys. J.* **71,** 403–409.
23. Lurie, D. J., Bussell, D. M., Bell, L. H. & Mallard, J. R. (1988) *J. Magn. Reson.* **76,** 366–370.
24. Krishna, M. C., English, S., Yamada, K., Yoo, J., Murugesan, R., Devasahayam, N., Cook, J. A., Golman, K., Ardenkjaer-Larsen, J. H., Subramanian, S. & Mitchell, J. B. (2002) *Proc. Natl. Acad. Sci. USA* **99,** 2216–2221.
25. Lurie, D. J., Li, H. H., Petryakov, S. & Zweier, J. L. (2002) *Magn. Reson. Med.* **47,** 181–186.
26. Golman, K., Petersson, J. S., Ardenkjaer-Larsen, J. H., Leunbach, I., Wistrand, L. G., Ehnholm, G. & Liu, K. (2000) *J. Magn. Reson. Imaging* **12,** 929–938.
27. Grucker, D., Guiberteau, T., Eclancher, B., Chambron, J., Chiarelli, R., Rassat, A., Subra, G. & Gallez, B. (1995) *J. Magn. Reson. B* **106,** 101–109.
28. Subramanian, S., Matsumoto, K., Mitchell, J. B. & Krishna, M. C. (2004) *NMR Biomed.* **17,** 263–294.
29. Golman, K., Ardenkjaer-Larsen, J. H., Petersson, J. S., Mansson, S. & Leunbach, I. (2003) *Proc. Natl. Acad. Sci. USA* **100,** 10435–10439.
30. Samuni, A., Goldstein, S., Russo, A., Mitchell, J. B., Krishna, M. C. & Neta, P. (2002) *J. Am. Chem. Soc.* **124,** 8719–8724.
31. Foster, M. A., Seimenis, I. & Lurie, D. J. (1998) *Phys. Med. Biol.* **43,** 1893–1897.
32. Metz, J. M., Smith, D., Mick, R., Lustig, R., Mitchell, J., Cherakuri, M., Glatstein, E. & Hahn, S. M. (2004) *Clin. Cancer Res.* **10,** 6411–6417.
33. Yamada, K., Nakamura, T. & Utsumi, H., *Free Radical Res.*, in press.
34. Sano, H., Matsumoto, K. & Utsumi, H. (1997) *Biochem. Mol. Biol. Int.* **42,** 641–647.
35. Sosnovsky, G. & Cai, Z. W. (1995) *J. Org. Chem.* **60,** 3414–3418.
36. Utsumi, H., Inoue, K., Nojima, S. & Kwan, T. (1978) *Biochemistry* **17,** 1990–1996.